

Spectral-infinite-element simulations of earthquake-induced gravity perturbations

Hom Nath Gharti ¹, Leah Langer ¹ and Jeroen Tromp ^{1,2}

¹*Department of Geosciences, Princeton University, Princeton, NJ 08544, USA. E-mail: hgharti@princeton.edu*

²*Program in Applied & Computational Mathematics, Princeton University, Princeton, NJ 08544-1000, USA*

Accepted 2019 January 15. Received 2019 January 11; in original form 2018 June 22

SUMMARY

Although earthquake-induced gravity perturbations are frequently observed, numerical modelling of this phenomenon has remained a challenge. Due to the lack of reliable and versatile numerical tools, induced-gravity data have not been fully exploited to constrain earthquake source parameters. From a numerical perspective, the main challenge stems from the unbounded Poisson/Laplace equation that governs gravity perturbations. Additionally, the Poisson/Laplace equation must be coupled with the equation of conservation of linear momentum that governs particle displacement in the solid. Most existing methods either solve the coupled equations in a fully spherical harmonic representation, which requires models to be (nearly) spherically symmetric, or they solve the Poisson/Laplace equation in the spherical harmonics domain and the momentum equation in a discretized domain, a strategy that compromises accuracy and efficiency. We present a spectral-infinite-element approach that combines the highly accurate and efficient spectral-element method with a mapped-infinite-element method capable of mimicking an infinite domain without adding significant memory or computational costs. We solve the complete coupled momentum-gravitational equations in a fully discretized domain, enabling us to accommodate complex realistic models without compromising accuracy or efficiency. We present several coseismic and post-earthquake examples and benchmark the coseismic examples against the Okubo analytical solutions. Finally, we consider gravity perturbations induced by the 1994 Northridge earthquake in a 3-D model of Southern California. The examples show that our method is very accurate and efficient, and that it is stable for post-earthquake simulations.

Key words: Geomechanics; Computational seismology; Earthquake dynamics; Gravity anomalies and Earth structure; Time variable gravity.

1 INTRODUCTION

Earthquake-induced gravity perturbations are frequently observed, in particular for large earthquakes (e.g. Chen *et al.* 2007; Panet *et al.* 2007; Matsuo & Heki 2011; Ozawa *et al.* 2012; Wang *et al.* 2012; Montagner *et al.* 2016; Whipple *et al.* 2016). These observations provide important constraints on the mechanics of earthquakes. However, due to a lack of reliable simulation tools for realistic 3-D earth models, earthquake-induced gravity data have thus far not been fully harnessed. The main challenge lies in solving the unbounded Poisson/Laplace equation—which governs the perturbed gravitational potential—in a discretized domain due the fact that an ‘unbounded domain’ and ‘discretization’ are generally incompatible. Coupling of the Poisson/Laplace equation with the equation of conservation of linear momentum further complicates the numerical procedure, especially for quasi-static problems.

The coupled momentum-gravitational equations are routinely solved for global problems, for example, for calculating the Earth’s free oscillations or to simulate glacial-isostatic adjustments. Most existing methods either solve the coupled equations entirely in the spherical harmonics domain or they solve the momentum equation in a discretized domain and the Poisson/Laplace equation in the spherical harmonics domain. The spherical harmonic normal-mode approach may be used to address problems in seismology (Takeuchi & Saito 1972; Dahlen & Tromp 1998), post-earthquake relaxation (Pollitz 1997) and glacial-isostatic adjustment (Tromp & Mitrovica 1999a,b; Spada *et al.* 2004). The closely related direct radial integration method is used to compute seismic displacements in spherically symmetric self-gravitating earth models (Al-Attar & Woodhouse 2008). Examples of the hybrid approach include spectral-element simulations of global seismic wave propagation (Chaljub & Valette 2004), glacial-isostatic adjustment using a finite-element method (Peltier *et al.* 1978; Zhong *et al.* 2003) or a 1-D spectral-element method (SEM; Al-Attar & Tromp 2014), and coseismic and post-earthquake deformation using a 1-D SEM (Crawford

et al. 2017). Other studies use a direct integral approach to solve Poisson/Laplace's equation combined with a discretized solution of the momentum equation (e.g. Latychev *et al.* 2005). The direct integral approach requires volume integration for each discretized point and is therefore computationally expensive.

Rundle (1980) solved the coupled elastic-gravitational equations in a layered half-space for point dislocations using a semi-analytical method. Okubo (1991, 1992) provided analytical expressions for gravity perturbations due to point and finite dislocations in a homogeneous Poisson solid. In this paper, the Obuku solutions will be used for benchmarking purposes. Sun & Okubo (1993, 1998) extended Obuku's analytical expressions to spherically symmetric earth models.

In order to simulate earthquake-induced gravity perturbations in realistic complex earth models, we must solve the coupled momentum-gravitational equations in a fully discretized domain. One seemingly simple approach to solve the unbounded Poisson/Laplace equation is to use a large model domain in an attempt to suppress boundary artefacts. However, this strategy requires large computational resources and generally results in only limited improvement (Tsynkov 1998). A better approach is to make use of infinite-element boundary conditions. In solid and fluid mechanics, the displacement descent approach (Bettest 1977; Medina & Taylor 1983; El-Esnawy *et al.* 1995) and the coordinate ascent approach (Beer & Meek 1981; Zienkiewicz *et al.* 1983; Kumar 1985; Angelov 1991) are both widely used to solve vanishing infinite boundary conditions. In the displacement descent approach, an element in the physical domain is mapped to an element in a natural domain of interval $[0, \infty]$. This is achieved by multiplying the standard interpolation functions by suitable decay functions. Since the integration interval is $[0, \infty]$, classical Gauss–Legendre quadrature cannot be employed. Either Gauss–Legendre quadrature has to be modified to accommodate the $[0, \infty]$ interval, or Gauss–Laguerre quadrature can be used (Mavriplis 1989). The Jacobian of the mapping and the numerical quadrature must be modified from the classical finite-element method. The coordinate ascent approach is also referred to as the ‘mapped infinite-element’ approach. In this technique, an element that extends to infinity in the physical domain is mapped to a standard natural element with interval $[-1, 1]$. This is achieved by defining shape functions using a reference point which serves as the pole of the decaying functions of choice. The corresponding shape functions possess singularities at the far end of the infinite element. Unlike in the displacement descent approach, only the Jacobian of the mapping must be modified, and quadrature identical to the classical finite-element method can be used.

To simulate earthquake-induced gravity perturbations, we use the spectral-infinite-element method (SIEM), which combines the infinite-element approach based on coordinate ascent with the SEM. The SEM is a higher-order finite-element method which uses nodal quadrature, specifically, Gauss–Legendre–Lobatto (GLL) quadrature. Due to the coincidence of the interpolation and quadrature points, pre- and post-processings are efficient and accurate. The method is widely used for dynamic problems, such as wave propagation (Faccioli *et al.* 1997; Seriani & Oliveira 2008; Tromp *et al.* 2008; Peter *et al.* 2011) and fluid dynamics (Patera 1984; Canuto *et al.* 1988; Deville *et al.* 2002), and also for quasi-static problems (Gharti *et al.* 2012a,b). For post-earthquake deformation problems, 1-D and 2.5-D SEMs are used, respectively, for spherically symmetric (Crawford *et al.* 2017) and axisymmetric models (Pollitz 2014).

Gharti *et al.* developed the SIEM and used it to calculate the gravity field of the Earth (Gharti & Tromp 2017), gravity anomalies for complex 3-D models (Gharti *et al.* 2018), and coseismic and post-earthquake deformation (Gharti *et al.* 2019). This paper details the development and implementation of the SIEM for earthquake-induced gravity perturbations. We focus on small or regional scale problems, which allows us to perform high-resolution simulations. We model coseismic and post-earthquake gravity perturbations for a variety of faults to illustrate and validate our method.

2 FORMULATION

2.1 Governing equation

We solve the coupled quasi-static momentum and Poisson/Laplace equations in a setting illustrated in Fig. 1. The governing equations in the domain of interest, Ω , are conservation of linear momentum,

$$\nabla \cdot \mathbf{T} + \nabla(\rho \mathbf{s} \cdot \mathbf{g}) - \nabla \cdot (\rho \mathbf{s}) \mathbf{g} - \rho \nabla \phi + \mathbf{f} = \mathbf{0} \quad \text{in} \quad \Omega, \quad (1)$$

and Poisson's equation,

$$(4\pi G)^{-1} \nabla^2 \phi + \nabla \cdot (\rho \mathbf{s}) = 0 \quad \text{in} \quad \Omega, \quad (2)$$

subject to the essential boundary conditions,

$$[\mathbf{s}]_{\pm}^{\pm} = \mathbf{0} \quad \text{on} \quad \Gamma, \quad (3)$$

$$[\phi]_{\pm}^{\pm} = 0 \quad \text{on} \quad \Gamma, \quad (4)$$

$$\mathbf{s} = \mathbf{0} \quad \text{on} \quad \Gamma_{\infty}, \quad (5)$$

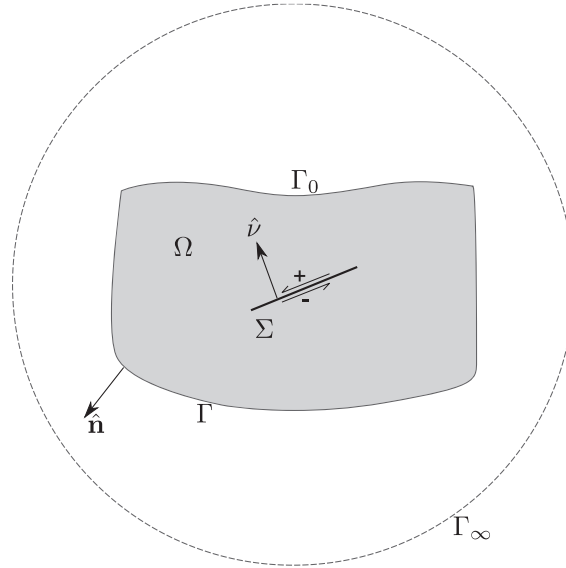


Figure 1. Schematic diagram of a fault buried in a domain of interest, Ω , embedded in a quasi-half-space. The embedded domain has a boundary consisting of a free surface Γ_0 and an artificial boundary Γ . The half-space has a boundary consisting of Γ_0 and a remainder Γ_∞ . The unit outward normal to the domain boundary is denoted by $\hat{\mathbf{n}}$. The domain Ω contains a fault surface Σ with unit normal $\hat{\mathbf{v}}$.

$$\phi = 0 \quad \text{on} \quad \Gamma_\infty, \quad (6)$$

and the natural boundary conditions,

$$[(4\pi G)^{-1} \hat{\mathbf{n}} \cdot \nabla \phi + \rho \hat{\mathbf{n}} \cdot \mathbf{s}]_\pm^+ = 0 \quad \text{on} \quad \Gamma, \quad (7)$$

$$[\hat{\mathbf{n}} \cdot \mathbf{T}]_\pm^+ = \mathbf{0} \quad \text{on} \quad \Gamma, \quad (8)$$

$$[(4\pi G)^{-1} \hat{\mathbf{n}} \cdot \nabla \phi]_\pm^+ + \rho \hat{\mathbf{n}} \cdot \mathbf{s} = 0 \quad \text{on} \quad \Gamma_0, \quad (9)$$

$$\hat{\mathbf{n}} \cdot \mathbf{T} = \mathbf{0} \quad \text{on} \quad \Gamma_0. \quad (10)$$

Here G denotes the universal gravitational constant, ρ the mass density, \mathbf{s} the displacement field, \mathbf{T} the incremental Lagrangian Cauchy stress and ϕ the perturbed gravitational potential. Similarly, $[\cdot]_\pm^+$ denotes the jump in the enclosed quantity when going from the $-$ side of boundary Γ to the $+$ side, and where $\hat{\mathbf{n}}$ denotes the unit outward normal to the boundary, pointing from the $-$ side to the $+$ side. The background gravitational potential Φ is governed by Poisson's equation:

$$\nabla^2 \Phi + 4\pi G \rho = 0. \quad (11)$$

Background gravitational acceleration is denoted by \mathbf{g} and is defined in terms of the gravitational potential Φ via $\mathbf{g} = -\nabla \Phi$.

Eqs (1) and (2) are coupled via the terms $-\rho \nabla \phi$ and $\nabla \cdot (\rho \mathbf{s})$. Coseismic deformation is controlled by the elastic constitutive relation $\mathbf{T} = \mathbf{c} : \boldsymbol{\varepsilon}$, where \mathbf{c} denotes the fourth-order elastic tensor and $\boldsymbol{\varepsilon}$ the strain tensor. Post-earthquake deformation is controlled by a generalized Maxwell rheology (Zienkiewicz & Taylor 2005)

$$\mathbf{T}(t) = \mathbf{c}^\infty : \boldsymbol{\varepsilon}(t) + \sum_{m=1}^M \mathbf{c}^m : \mathbf{q}^m(t), \quad (12)$$

where η^m represents the viscosity of the m th dashpot and M the total number of parallel Maxwell elements as shown in Fig. 2. The elastic modulus of the elastic element is denoted by \mathbf{c}^∞ , and \mathbf{c}^m denotes the elastic modulus of the m th Maxwell element, so that the total modulus \mathbf{c} is determined by

$$\mathbf{c} = \mathbf{c}^\infty + \sum_{m=1}^M \mathbf{c}^m. \quad (13)$$

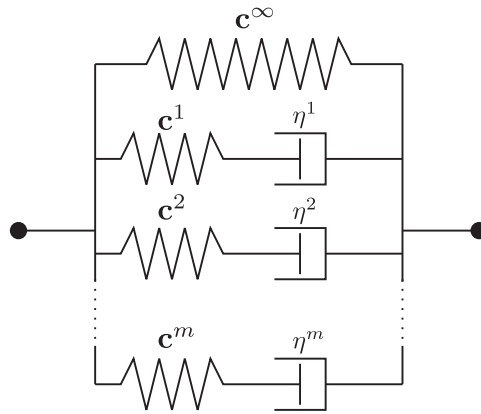


Figure 2. Schematic diagram of the generalized Maxwell rheology.

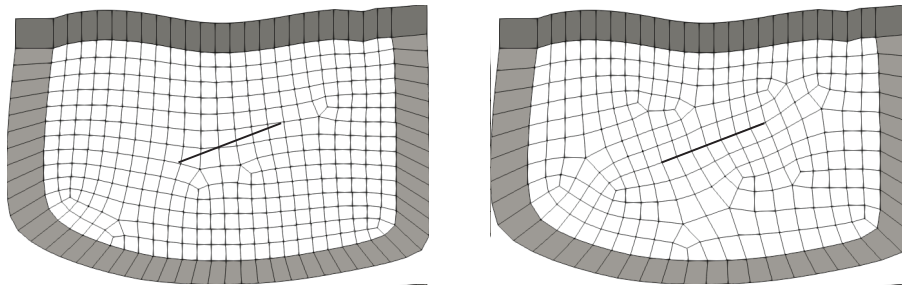


Figure 3. The domain of interest, Ω , is discretized using spectral elements (white). A single layer of infinite elements is added outside the domain. Light grey: infinite elements radiating from the lateral and bottom surfaces have both the displacement and the gravity degrees of freedom. Dark grey: infinite elements radiating from the free surface have only the gravity degree of freedom. Left: mesh does not honour the fault. Right: mesh honours the fault.

The Maxwell rheology is a special case, for which $\mathbf{c}^\infty = \mathbf{0}$ and $m = 1$. The partial strain $\mathbf{q}^m(t)$ is the solution to the first-order differential equation

$$\dot{\mathbf{q}}^m + \mathbf{q}^m / \tau^m = \dot{\boldsymbol{\epsilon}}, \tag{14}$$

where $\tau^m = \eta^m / E^m$ denotes the relaxation time and E^m the Young’s modulus of the m th Maxwell element. We use a second-order unconditionally stable recurrence integration algorithm for the general Maxwell rheology, as described in Gharti *et al.* (2019).

The earthquake source is implemented either based on a moment-density tensor or a split-node approach, as discussed in Gharti *et al.* (2019) and illustrated in Fig. 3. In the moment-density tensor approach, an external body force is imposed by computing an equivalent moment-density tensor from the prescribed slip of the source. Since the equivalent body force is imposed, the mesh is not necessarily required to honour the fault surface, as shown in Fig. 3 (left). However, in the split-node approach, the mesh must honour the fault surface, as shown in Fig. 3 (right), and slip is explicitly prescribed on the split nodes.

2.2 Weak form

We define a test vector \mathbf{w} for the displacement field and a test function w for the perturbed gravitational potential. The weak form of the momentum eq. (1) may be obtained by taking the dot product with the test vector \mathbf{w} and integrating over the domain of interest Ω , and the weak form of Poisson’s eq. (2) may be obtained by multiplying by the scalar test function w and integrating over all of space \mathcal{O} . Using Gauss’ theorem, we obtain

$$\int_{\Omega} \nabla \mathbf{w} : \mathbf{T} \, dV - \int_{\Omega} \mathbf{w} \cdot [\nabla (\rho \mathbf{s} \cdot \mathbf{g}) - \nabla \cdot (\rho \mathbf{s}) \mathbf{g}] \, dV + \int_{\Omega} \rho \mathbf{w} \cdot \nabla \phi \, dV = \int_{\Omega} \mathbf{w} \cdot \mathbf{f} \, dV + \int_{\Gamma} \mathbf{w} \cdot \mathbf{T} \cdot \hat{\mathbf{n}} \, dS, \tag{15}$$

and

$$\int_{\Omega} \rho \nabla w \cdot \mathbf{s} \, dV + (4\pi G)^{-1} \int_{\mathcal{O}} \nabla w \cdot \nabla \phi \, dV = \int_{\Gamma} w [(4\pi G)^{-1} \hat{\mathbf{n}} \cdot \nabla \phi + \rho \hat{\mathbf{n}} \cdot \mathbf{s}] \, dS. \tag{16}$$

Al-Attar & Tromp (2014) have shown that the second integral in the weak form (15) can be expressed in an explicitly symmetric form, assuming that level surfaces of ρ and Φ coincide in hydrostatic equilibrium. Consequently, the final weak form of eq. (15) is

$$\begin{aligned} \int_{\Omega} \nabla \mathbf{w} : \mathbf{T} dV - \frac{1}{2} \int_{\Omega} \rho [\mathbf{w} \cdot \nabla (\mathbf{s} \cdot \mathbf{g}) + \nabla (\mathbf{w} \cdot \mathbf{g}) \cdot \mathbf{s}] dV + \frac{1}{2} \int_{\Omega} \rho [\mathbf{w} \cdot \mathbf{g} \nabla \cdot \mathbf{s} + \nabla \cdot \mathbf{w} \mathbf{s} \cdot \mathbf{g}] dV \\ + \int_{\Omega} \rho \mathbf{w} \cdot \nabla \phi dV = \int_{\Omega} \mathbf{w} \cdot \mathbf{f} dV + \int_{\Gamma} \mathbf{w} \cdot \mathbf{T} \cdot \hat{\mathbf{n}} dS. \end{aligned} \quad (17)$$

2.3 Discretization

To solve the weak form of the coupled momentum-gravitational eqs (16) and (17), the domain Ω is meshed using spectral elements. A single layer of infinite elements is added outside the domain to reproduce the behaviour of outer space, as shown in Fig. 3. As discussed in Gharti *et al.* (2018, 2019), spectral and infinite elements share the same interpolation functions, namely Lagrange polynomials, but use different quadrature. Thus, the displacement field \mathbf{s} is discretized in natural coordinates ξ as

$$\mathbf{s}(\xi) = \sum_{\alpha=1}^n \mathbf{s}_{\alpha} N_{\alpha}(\xi), \quad (18)$$

and the perturbed gravitational potential ϕ is discretized as

$$\phi(\xi) = \sum_{\alpha=1}^n \phi_{\alpha} N_{\alpha}(\xi), \quad (19)$$

where \mathbf{s}_{α} and ϕ_{α} denote the displacement and perturbed gravity potential, respectively, at quadrature point ξ_{α} , and N_{α} is an interpolation function. The total number of quadrature points in an element is denoted by n and is given by the product of the number of quadrature points in each dimension, n^j , $j = 1, 2, 3$; that is, $n = \prod_{j=1}^3 n^j$. The interpolation functions N_{α} in natural coordinates are determined by a tensor product of 1-D Lagrange polynomials, that is,

$$N_{\alpha}^j(\xi^j) = \prod_{\substack{\beta=1 \\ \beta \neq \alpha^j}}^{n^j} \frac{(\xi^j - \xi_{\beta}^j)}{(\xi_{\alpha}^j - \xi_{\beta}^j)}, \quad (20)$$

such that

$$N_{\alpha}(\xi) = \prod_{j=1}^3 N_{\alpha}^j(\xi^j). \quad (21)$$

Here α denotes the index of quadrature point $\xi_{\alpha} = \{\xi_{\alpha^1}, \xi_{\alpha^2}, \xi_{\alpha^3}\}$.

Components of the test vector \mathbf{w} and the test function w are taken to be an interpolation function N_{α} , making the approach a Galerkin method. Upon substituting such a test vector and the displacement field given by eq. (18) in eq. (17), and a test function and the gravity field given by eq. (19) in eq. (16), we obtain a set of elemental linear equations that may be written in the matrix-vector form

$$\begin{bmatrix} \mathbf{K}_e^{\text{ss}} & \mathbf{K}_e^{\text{s}\phi} \\ \mathbf{K}_e^{\phi\text{s}} & \mathbf{K}_e^{\phi\phi} \end{bmatrix} \begin{bmatrix} \mathbf{S}_e \\ \Phi_e \end{bmatrix} = \begin{bmatrix} \mathbf{F}_e^{\text{s}} \\ \mathbf{F}_e^{\phi} \end{bmatrix}. \quad (22)$$

The submatrices \mathbf{K}_e^{ss} , $\mathbf{K}_e^{\text{s}\phi}$, $\mathbf{K}_e^{\phi\text{s}}$ and $\mathbf{K}_e^{\phi\phi}$ are the components of the unified stiffness matrix. The diagonal submatrices \mathbf{K}_e^{ss} and $\mathbf{K}_e^{\phi\phi}$ represent contributions solely from the displacement and perturbed gravity potential, respectively. The off-diagonal submatrices represent coupling between the displacement and the perturbed gravity potential. The subvectors \mathbf{F}_e^{s} and \mathbf{F}_e^{ϕ} represent the displacement and perturbed gravity potential force vectors, respectively.

The elemental displacement vector, \mathbf{S}_e , has the form

$$\mathbf{S}_e = \left[s_1^x \quad s_1^y \quad s_1^z \quad s_2^x \quad s_2^y \quad s_2^z \quad s_3^x \quad s_3^y \quad s_3^z \quad \cdots \quad s_n^x \quad s_n^y \quad s_n^z \right]^T, \quad (23)$$

with $3n$ entries for the three components of displacement at each of the n quadrature points. Similarly, the elemental perturbed potential vector, Φ_e , has the form

$$\Phi_e = \left[\phi_1 \quad \phi_2 \quad \phi_3 \quad \cdots \quad \phi_n \right]^T, \quad (24)$$

with n entries for the perturbed gravity potential at the n quadrature points. The transpose of a vector or matrix is denoted by T . Symbolically, we may write the elemental stiffness matrix components and the force vectors as

$$\mathbf{K}_e^{\text{ss}} = \int_{\Omega_e} \mathbf{B}_e^{\text{sT}} \mathbf{C} \mathbf{B}_e^{\text{s}} dV - \frac{1}{2} \int_{\Omega_e} \rho \left[\mathbf{N}_e^{\text{s}} (\mathbf{H}_e + \mathbf{N}_e^{\text{s}} \mathbf{G})^T + (\mathbf{H}_e + \mathbf{N}_e^{\text{s}} \mathbf{G}) \mathbf{N}_e^{\text{sT}} \right] dV + \frac{1}{2} \int_{\Omega_e} \rho \left[(\mathbf{g} \mathbf{N}_e^{\text{sT}})^T (\mathbf{d}^T \mathbf{N}_e^{\text{sT}}) + (\mathbf{d}^T \mathbf{N}_e^{\text{sT}})^T \mathbf{g} \mathbf{N}_e^{\text{sT}} \right] dV, \quad (25)$$

$$\mathbf{K}_e^{s\phi} = \int_{\Omega_e} \rho \mathbf{N}_e^s \mathbf{B}_e^\phi dV, \tag{26}$$

$$\mathbf{K}_e^{\phi s} = \int_{\Omega_e} \rho \mathbf{B}_e^{\phi T} \mathbf{N}_e^{sT} dV = \mathbf{K}_e^{s\phi T}, \tag{27}$$

$$\mathbf{K}_e^{\phi\phi} = (4\pi G)^{-1} \int_{\Omega_e} \mathbf{B}_e^{\phi T} \mathbf{B}_e^\phi dV. \tag{28}$$

Here Ω_e denotes element e , and \mathbf{C} denotes the 3-D elasticity tensor stored as a 6×6 matrix. The gradient of the background gravity, $\mathbf{G} = \nabla \mathbf{g}$, is symmetric, and \mathbf{H}_e denotes the outer product between a differential operator and the interpolation function matrix dotted with the background gravity, that is,

$$\mathbf{H}_e = \begin{bmatrix} \frac{\partial \mathbf{N}_e}{\partial x} \mathbf{g} & \frac{\partial \mathbf{N}_e}{\partial y} \mathbf{g} & \frac{\partial \mathbf{N}_e}{\partial z} \mathbf{g} \end{bmatrix}. \tag{29}$$

The strain-displacement matrix, \mathbf{B}_e^s , is given by

$$\mathbf{B}_e^s = \mathbf{D} \mathbf{N}_e^{sT}, \tag{30}$$

and the gravity-potential matrix, \mathbf{B}_e^ϕ , is given by

$$\mathbf{B}_e^\phi = \mathbf{d} \mathbf{N}_e^{\phi T}, \tag{31}$$

where we have defined the differential matrix operator

$$\mathbf{D} = \begin{bmatrix} \frac{\partial}{\partial x} & 0 & 0 \\ 0 & \frac{\partial}{\partial y} & 0 \\ 0 & 0 & \frac{\partial}{\partial z} \\ \frac{\partial}{\partial y} & \frac{\partial}{\partial x} & 0 \\ 0 & \frac{\partial}{\partial z} & \frac{\partial}{\partial y} \\ \frac{\partial}{\partial z} & 0 & \frac{\partial}{\partial x} \end{bmatrix} \tag{32}$$

and the differential vector operator

$$\mathbf{d} = \begin{bmatrix} \frac{\partial}{\partial x} \\ \frac{\partial}{\partial y} \\ \frac{\partial}{\partial z} \end{bmatrix}. \tag{33}$$

The interpolation function matrix for the displacement field is defined as

$$\mathbf{N}_e^s = \begin{bmatrix} N_1 & 0 & 0 & N_2 & 0 & 0 & N_3 & 0 & 0 & \dots & N_n & 0 & 0 \\ 0 & N_1 & 0 & 0 & N_2 & 0 & 0 & N_3 & 0 & \dots & 0 & N_n & 0 \\ 0 & 0 & N_1 & 0 & 0 & N_2 & 0 & 0 & N_3 & \dots & 0 & 0 & N_n \end{bmatrix}^T \tag{34}$$

and the interpolation function vector for the gravity potential is defined as

$$\mathbf{N}_e^\phi = [N_1 \quad N_2 \quad N_3 \quad \dots \quad N_n]^T. \tag{35}$$

The gravity potential force vector \mathbf{F}_e^ϕ takes the following form:

$$\mathbf{F}_e^\phi = (4\pi G)^{-1} \int_{\Gamma_\infty} \mathbf{N}_e^\phi g_n dS, \tag{36}$$

where $g_n = \hat{\mathbf{n}} \cdot \nabla \phi$ denotes the normal component of the perturbed gravity. As shown by Gharti *et al.* (2019), the displacement force vector takes different forms depending on the earthquake source implementation. For the split-node approach it takes the form

$$\mathbf{F}_e^s = -\frac{1}{2} (\mathbf{K}_e^{ss+} - \mathbf{K}_e^{ss-}) \Delta \mathbf{S}_e + \int_{\Gamma_0} \mathbf{N}_e^s \mathbf{t} dS, \tag{37}$$

and for the moment-density tensor approach it takes the form

$$\mathbf{F}_e^s = \mathcal{N}^T \mathbf{M} + \int_{\Gamma_0} \mathbf{N}_e^s \mathbf{t} dS. \quad (38)$$

Eqs (36)–(38) represent the general form of the force vector. However, the surface integral on the surface at infinity does not have to be computed due to the Dirichlet boundary conditions. Similarly, the surface integral on the free surface does not have to be computed if there is no externally applied traction. The elemental slip vector, $\Delta \mathbf{S}_e$ has non-zero values only on fault surface nodes. Similarly, the matrices \mathbf{K}_e^{ss+} and \mathbf{K}_e^{ss-} are evaluated on the + and – sides of the fault surface, respectively. The traction vector $\mathbf{t} = \mathbf{T} \cdot \hat{\mathbf{n}}$ is defined by

$$\mathbf{t} = \begin{bmatrix} t^x & t^y & t^z \end{bmatrix}^T. \quad (39)$$

The outer product between the differential vector operator \mathbf{d} and the interpolation function matrix \mathbf{N}_e^s is given by

$$\mathcal{N} = \begin{bmatrix} \frac{\partial \mathbf{N}_e}{\partial x} & \frac{\partial \mathbf{N}_e}{\partial y} & \frac{\partial \mathbf{N}_e}{\partial z} \end{bmatrix}. \quad (40)$$

The moment-density tensor matrix is represented by a nine-component column vector as

$$\mathbf{M} = \begin{bmatrix} m_{11} & m_{12} & m_{13} & m_{21} & m_{22} & m_{23} & m_{31} & m_{32} & m_{33} \end{bmatrix}^T, \quad (41)$$

where, m_{ij} , $i, j = 1, 2, 3$ are the components of the symmetric moment-density tensor, \mathbf{m} .

After assembling the elemental matrices and vectors, we obtain a set of global linear equations

$$\begin{bmatrix} \mathbf{K}^{ss} & \mathbf{K}^{s\phi} \\ \mathbf{K}^{\phi s} & \mathbf{K}^{\phi\phi} \end{bmatrix} \begin{bmatrix} \mathbf{S} \\ \Phi \end{bmatrix} = \begin{bmatrix} \mathbf{F}^s \\ \mathbf{F}^\phi \end{bmatrix}, \quad (42)$$

where \mathbf{K}^{ss} , $\mathbf{K}^{s\phi}$, $\mathbf{K}^{\phi s}$ and $\mathbf{K}^{\phi\phi}$ are submatrices of the symmetric global stiffness matrix. The subvectors \mathbf{F}^s and \mathbf{F}^ϕ are the global force vectors associated with the displacement and perturbed gravity potential, respectively. Similarly, \mathbf{S} is the global displacement vector and Φ the global perturbed gravity potential vector. These vectors are simultaneously determined by solving the system of linear equation (42).

As described in detail in Gharti *et al.* (2019), in spectral elements, we use GLL quadrature to construct the stiffness matrix, whereas in infinite elements we use Gauss–Radau quadrature. Quadrature points on a geoid anomaly spectral-infinite element interface coincide, thereby naturally coupling the two domains.

3 EXAMPLES

We rely on MeshAssist (Gharti *et al.* 2017) and Trelis/CUBIT (CUBIT 2017) for model preparation and meshing for all examples included in this paper. All simulations use 3 GLL points in each direction resulting in a total of 27 points per element.

3.1 Coseismic gravity perturbation

In the following examples, we compute coseismic gravity perturbations and compare with the corresponding Okubo solutions. We adapted the open source package ‘OKUBO’ (Beauducel 2013), originally developed by François Beauducel and later modified by Taco Broerse, to calculate the reference solutions. We note that the Okubo analytical expressions depend only on a single elastic parameter, namely, Poisson’s ratio.

3.1.1 Vertical strike-slip fault

We consider a homogeneous model of size 100 km × 80 km × 52 km with a vertical fault of size 20 km × 10 km, as shown in Fig. 4. The centre of the fault is located at 7 km depth. We use homogeneous material properties with a Young’s modulus of 5.68×10^{10} N m⁻², a Poisson’s ratio of 0.25 and a mass density of 2670 kg m⁻³.

Since the farthest extent of the infinite-element layer lies virtually at infinity, the numerical derivative in the infinite elements may not be accurate. Therefore, to be conservative, we add a transition layer of thickness equal to the average element size on top of the free surface. The model is meshed using hexahedral elements with an average size of 2 km, resulting in a total of 62 860 spectral elements, 520 839 quadrature points and 1 866 879 degrees of freedom. The mesh honours the fault surface, as shown in Fig. 5 (left). This is essential for the split-node approach but not for the moment-density tensor approach (Gharti *et al.* 2019). Note, however, that a mesh designed for the split-node approach can also be used for the moment-density tensor approach. A single layer of infinite elements is added outside the model surfaces, as shown in Fig. 5 (right). The transition layer involves only the gravity degrees of freedom, and all other elements involve both the displacement and gravity degrees of freedom. There are 8860 infinite elements, comprising about 14 per cent of the total number of elements. Note that the mesh in the infinite-element layer satisfies the non-converging condition at infinity, since opposite faces diverge. We take the centre of the source as the pole position for the infinite-element mapping (Gharti *et al.* 2019).

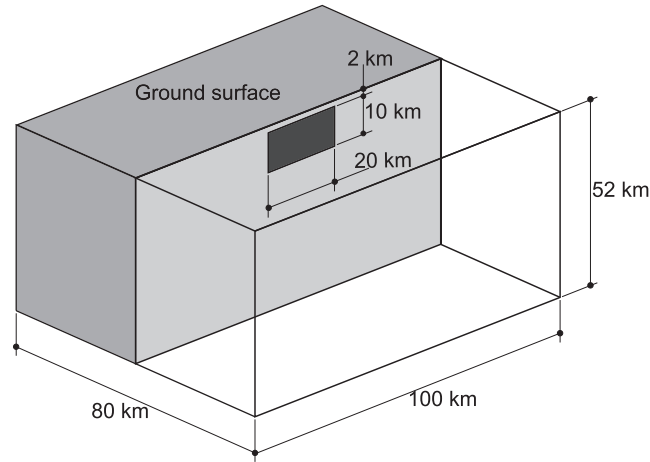


Figure 4. Model geometry for a vertical fault. The model is cut along the fault plane (dark grey).

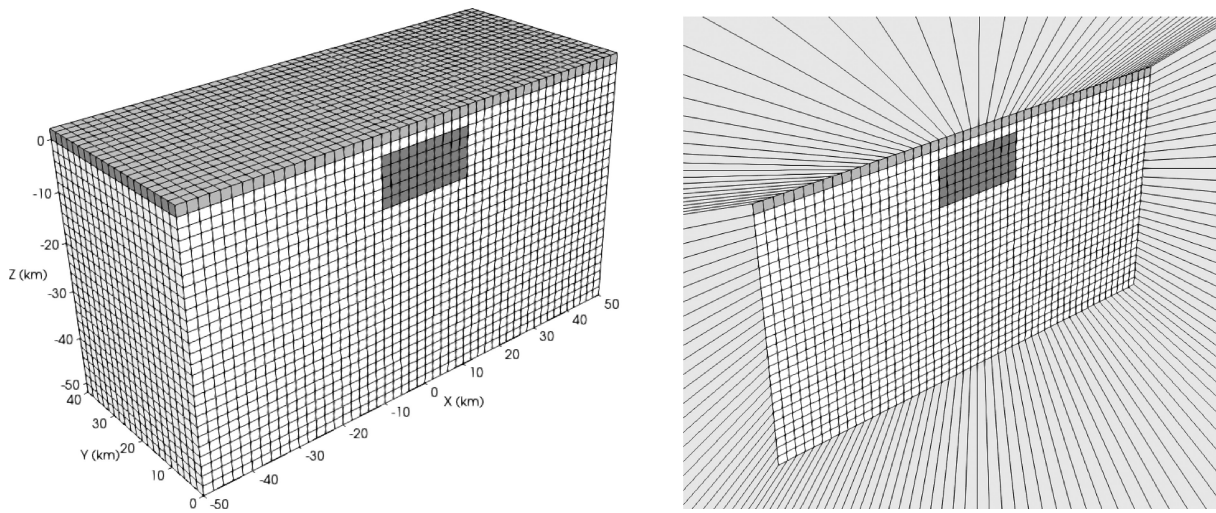


Figure 5. Left: spectral-element mesh of a vertical fault model. The model is cut along the fault (dark grey). Right: infinite elements radiating from the outer surfaces of the model (grey). A transition layer is added on top of the free surface (light grey).

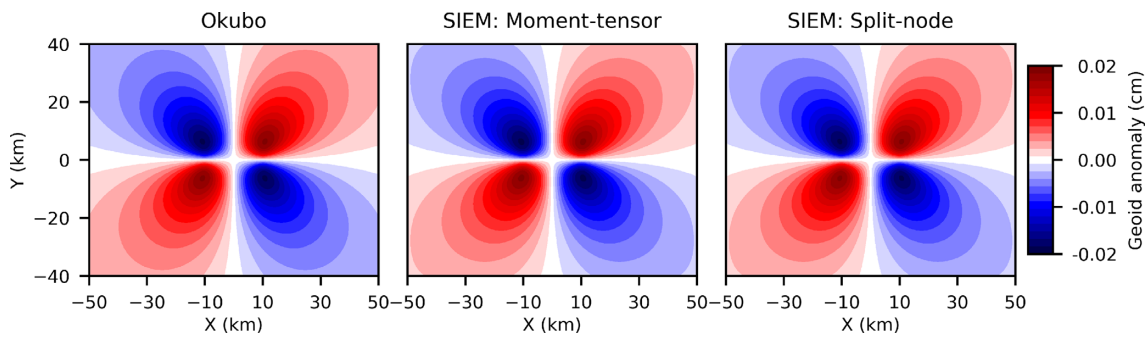


Figure 6. Geoid anomaly computed on the free surface for the vertical strike-slip fault. Left to right: Okubo analytical solution, SIEM with moment-density tensor approach and SIEM with split-node approach.

A vertical strike-slip source is defined by a 5-m slip along strike. The slip is equivalent to a scalar seismic moment of $M_0 \approx 2.2720 \times 10^{19}$ N m, or a moment magnitude of $M_w \approx 6.87$. Dirichlet boundary conditions are imposed at infinity, such that the displacement and gravity potential decay to zero at infinity. We perform simulations with both the moment-density tensor and the split-node approaches.

In Fig. 6, we plot the geoid anomaly on the free surface and compare it with the Okubo analytical solution. The geoid anomaly is defined by the perturbed gravitational potential divided by the background gravity, $\phi/\|\mathbf{g}\|$, giving it a unit of metres. The numerical results are in good agreement with the Okubo solution. The main lobes around the source are nicely reproduced by the two SIEM solutions. We observe a geoid anomaly up to $\approx \pm 0.2$ mm. For closer inspection, we plot a gravity potential profile along the x -axis at $y = -6$ km, shown in Fig. 7.

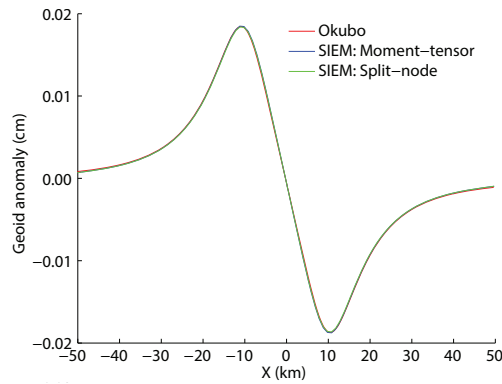


Figure 7. Profiles of the geoid anomaly for the vertical strike-slip fault plotted along the x -axis at $y = -6$ km on the top surface.

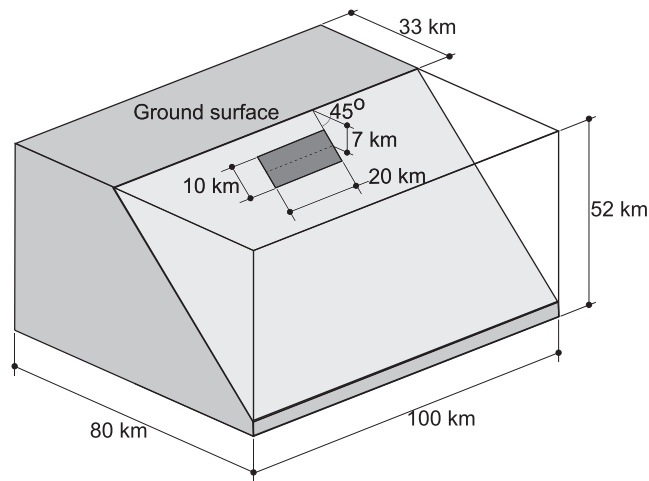


Figure 8. Model geometry of the inclined fault. The model is cut along the fault plane (dark grey).

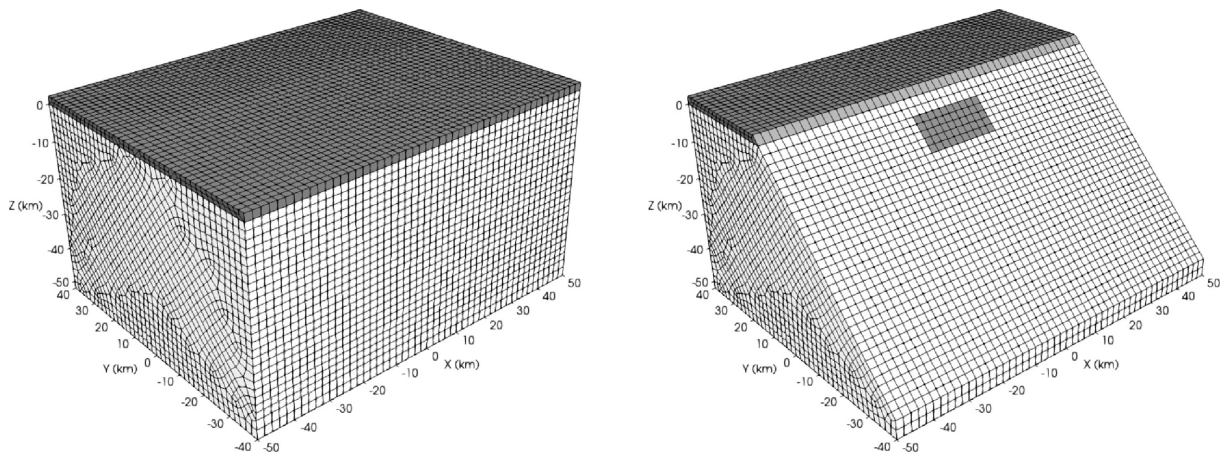


Figure 9. Left: spectral-element mesh for an inclined fault model. Right: the model is cut along the fault plane (dark grey). A transition layer is added on top of the free surface (light grey).

We observe that the numerical results are in very good agreement with the Okubo solution.

3.1.2 Inclined strike-slip fault

In this example, we consider the same model domain as in the previous example. The fault has the same size and location, but dips at a 45° angle, as shown in Fig. 8. We impose 5 m of slip along strike. To honour the fault surface, we cut the entire model through the fault plane. We add a transition layer on top of the free surface. We mesh the model using hexahedral elements with an average size of 2 m, as shown in Fig. 9. A single layer of infinite elements is added. The mesh consists of 66 392 elements, 549 561 quadrature points and 1 924 337 degrees

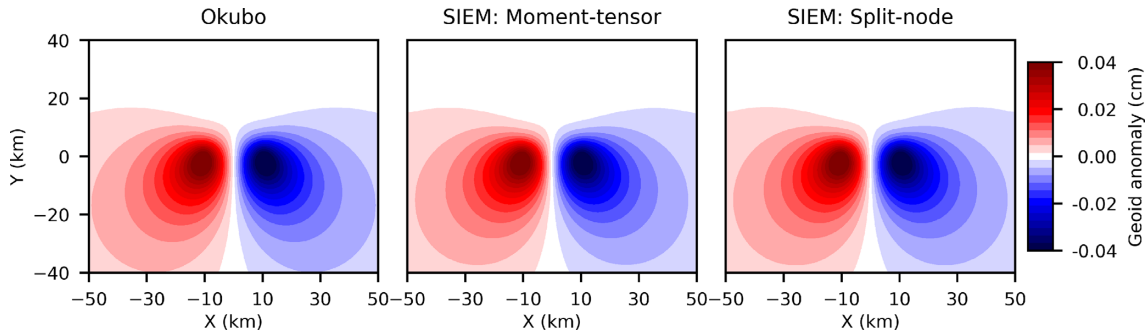


Figure 10. Geoid anomaly computed on the free surface for the inclined strike-slip fault. Left to right: Okubo analytical solution, SIEM with moment-density tensor approach and SIEM with split-node approach.

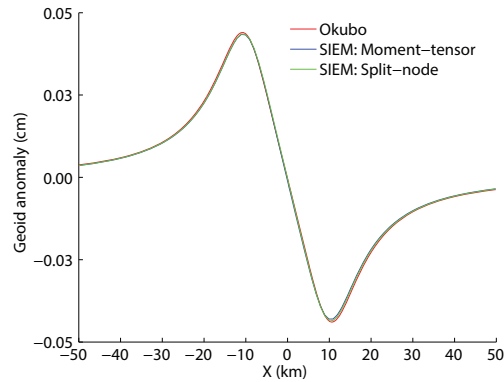


Figure 11. Profiles of the geoid anomaly for the inclined fault plotted along the x -axis at $y = -2$ km on the top surface.

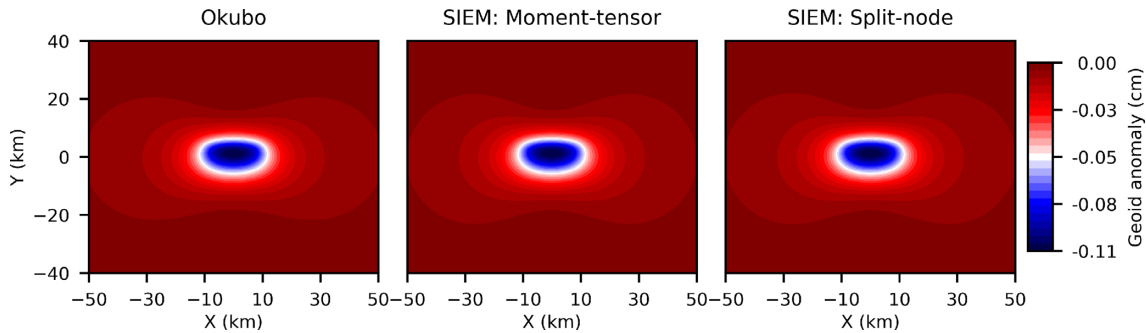


Figure 12. Geoid anomaly computed on the free surface for an inclined thrust fault. Left to right: Okubo analytical solution, SIEM with moment-density tensor approach and SIEM with split-node approach.

of freedom. There are 9092 infinite elements, which is about 14 per cent of the total number of elements.

We perform simulations with both the moment-density tensor and split-node approaches. Maps of the gravity potential field computed on the free surface are shown in Fig. 10. The numerical results are in good agreement with the analytical solution. Both approaches are capable of reproducing the major features of the geoid anomaly pattern accurately. We observe that the geoid anomaly is larger than in the vertical strike-slip case due to larger surface displacements. The largest geoid anomalies observed on the free surface are $\approx \pm 0.4$ mm. It is interesting to note that the geoid anomaly almost doubles when the dip angle is changed to 45° , even though the fault characteristics are otherwise identical. For closer inspection, we plot profiles of the gravity potential on the free surface along the x -axis at $y = -2$ km, as shown in Fig. 11. Both the moment-density tensor and the split-node results match the Okubo analytical solution very well.

3.1.3 Inclined thrust fault

In this example, we consider the same model domain and mesh as in the previous examples. In this case, we define a thrust fault with 5 m of slip. We perform simulations with both the moment-density tensor and split-node approaches. Resulting maps of the geoid anomaly computed on the free surface are shown in Fig. 12. The numerical results are in good agreement with the analytical solution, and both methods are capable of reproducing the major features of the radiation pattern. We observe drastically larger geoid anomalies than in the previous examples. The positive geoid anomaly computed on the free surface is as large as ≈ 1.1 mm. The negative anomaly is negligible on the

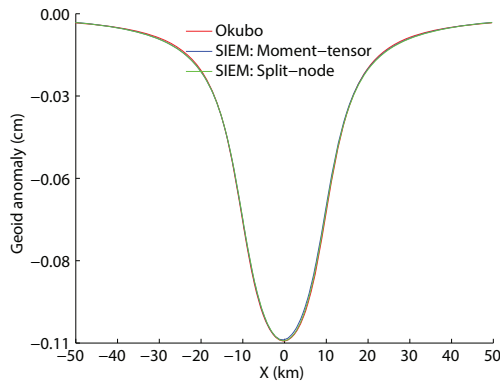


Figure 13. Profiles of the geoid anomaly for the inclined thrust fault plotted along the x -axis at $y = 1$ km on the top surface.

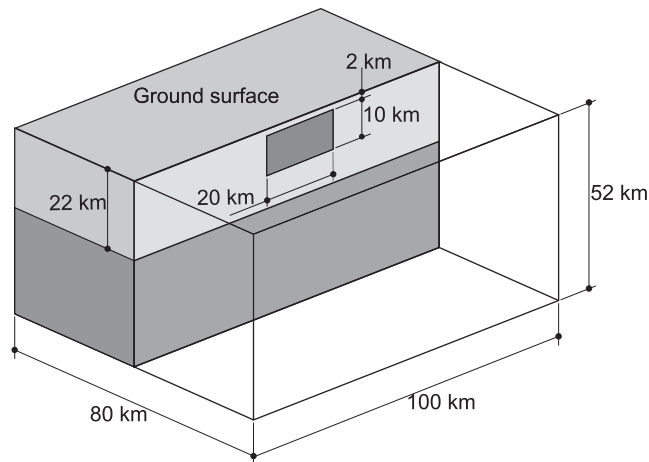


Figure 14. Model geometry for a vertical fault in a viscoelastic model. The model is cut along the fault plane (dark grey). The model consists of an upper elastic layer (light grey) and a lower viscous layer (dark grey).

surface. It is again interesting to see that the geoid anomaly is drastically different even though we have only changed the slip direction. The geoid anomaly is almost three times larger than in the case with slip along the strike direction. For closer inspection, we plot profiles for each solution on the free surface along the x -axis at $y = 1$ km, as shown in the Fig. 13. Both numerical results are in good agreement with the analytical solution.

3.2 Post-earthquake gravity perturbation

In the following examples, we perform viscoelastic simulations using a Maxwell rheology.

3.2.1 Vertical strike-slip fault

We consider a model of size $100 \text{ km} \times 80 \text{ km} \times 52 \text{ km}$ with a vertical fault of size $20 \text{ km} \times 10 \text{ km}$, as shown in Fig. 14. The model consists of a viscoelastic layer of thickness 30 km overlain by a 22 km thick elastic layer. The centre of the fault is located at 7 km depth. We use homogeneous material properties with a Young's modulus of $5.68 \times 10^{10} \text{ N m}^{-2}$, a Poisson's ratio of 0.25 and a mass density of 2670 kg m^{-3} . The viscoelastic layer has a viscosity of $\eta = 7.1 \times 10^{19} \text{ Pa s}$. We add a transition layer on the top of the free surface. The model is meshed using hexahedral elements with an average size of 2 km. The mesh, shown in Fig. 15, honours the fault surface. The mesh consists of 62 860 spectral elements, 520 839 quadrature points and 1 866 879 degrees of freedom. A single layer of infinite elements surrounds the model. There are 8860 infinite elements, comprising about 14 per cent of the total number of elements. Due to the viscoelastic layer, there are three types of infinite elements: empty infinite elements, which radiate from the transition layer surfaces and carry only the gravity potential degrees of freedom; elastic infinite elements, which radiate from the elastic layer surfaces and carry both the displacement and gravity potential degrees of freedom; and viscoelastic infinite elements, which radiate from the viscoelastic layer surfaces and carry both the displacement and gravity potential degrees of freedom. All infinite elements inherit their material properties from the parent elements.

We impose 5 m of slip along strike. We perform viscoelastic simulations using the moment-density tensor and split-node approaches for 300 yr using a time step of 10 yr. We use the vanishing Dirichlet boundary condition at infinity and set zero initial conditions.

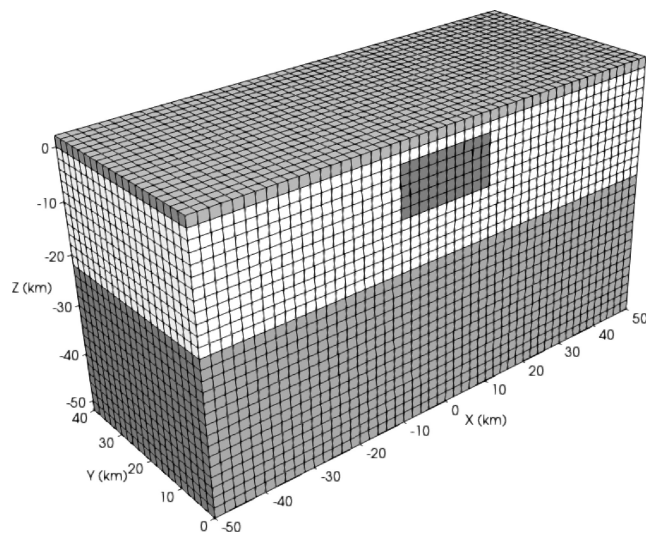


Figure 15. Spectral-element mesh for a vertical fault model. The model is cut along the fault plane (dark grey). A transition layer is added on top of the free surface (light grey).

Snapshots of the geoid anomaly computed on the free surface at 0, 100, 200 and 300 yr are shown in Fig. 16. The moment-density tensor and split-node approaches give very similar results. Amplitudes of the positive and negative geoid anomalies gradually decay with time. After 300 yr, the geoid anomaly observed on the free surface decays from $\approx \pm 0.2$ to $\approx \pm 0.17$ mm.

3.2.2 Inclined strike-slip fault

In this example, we use the same model as in the previous example, but the fault dips at 45° , as shown in Fig. 17.

We add a transition layer on top of the free surface and mesh the model using hexahedral elements with an average size of 2 km. The mesh, shown in Fig. 18, honours the fault surface. The mesh consists of 65 972 spectral elements, 546 363 quadrature points and 1 910 265 degrees of freedom. A single layer of infinite elements surrounds the model. There are 9172 infinite elements, which represent about 14 per cent of the total elements.

We impose 5 m of slip along strike and perform viscoelastic simulations using both the moment-density tensor and split-node approaches for 300 yr using a time step of 10 yr. We use the vanishing Dirichlet boundary condition at infinity and zero initial conditions.

Snapshots of the geoid anomaly computed on the free surface at 0, 100, 200 and 300 yr are shown in Fig. 19. The moment-density tensor and split-node approaches give very similar results. We observe that the amplitudes of the positive and negative geoid anomalies gradually increase with time. After 300 yr, the geoid anomaly on the free surface increases from $\approx \pm 0.40$ to $\approx \pm 0.51$ mm.

3.2.3 Inclined thrust fault

In this example, we consider the same model domain and mesh as in the previous examples.

We impose 5 m of slip on a thrust fault and perform viscoelastic simulations using both the moment-density tensor and split-node approaches for 300 yr using a time step of 10 yr. We use the vanishing Dirichlet boundary condition at infinity and zero initial conditions.

Snapshots of the geoid anomaly computed on the free surface at 0, 100, 200 and 300 yr are shown in Fig. 20. The moment-density tensor and split-node approaches give very similar results. Negative geoid anomalies decay with time while the positive geoid anomaly increases with time. After 300 yr, negative anomalies on the free surface decrease from ≈ 1.10 to ≈ 0.87 mm and positive anomalies on the free surface increase from ≈ 0.00 to ≈ 0.13 mm.

3.3 1994 Northridge earthquake

To demonstrate the applicability of our method to real problems, we compute coseismic gravity perturbations due to the 1994 January 17 Northridge ($M_w = 6.7$) earthquake. The epicentre is located at (34.211° latitude, -118.546° longitude) and the hypocentral depth is 17.5 km. The finite source corresponding to the earthquake (Wald *et al.* 1996) is described by 14 700 moment-density tensor sources. We use the 3-D Southern California model by Tape *et al.* (2009).

The model size is $666 \text{ km} \times 503 \text{ km} \times 400 \text{ km}$. Bathymetry and topography vary from -4209 m to 3915 m . The mesh consists of 1 272 068 elements and honours the free surface topography, as shown in Fig. 21 (left). The element size varies from $\approx 12.33 \text{ km}$ on the bottom to $\approx 1.37 \text{ km}$ on the top. To facilitate the creation of the infinite elements on the free surface, we added a transition layer, as shown in Fig. 21

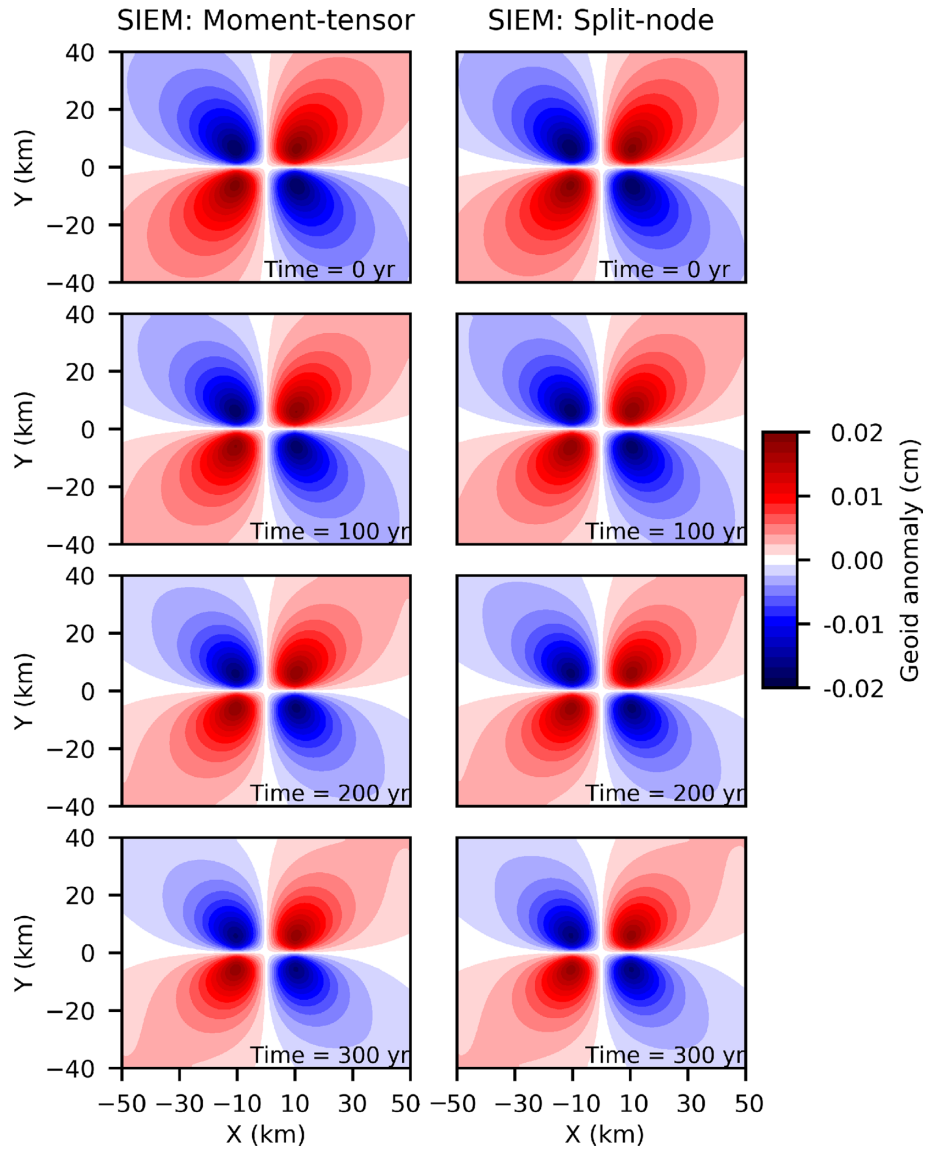


Figure 16. Geoid anomaly for a vertical strike-slip fault computed on the free surface at 0, 100, 200 and 300 yr after the earthquake (top to bottom). Left column: SIEM based on the moment-density tensor approach. Right column: SIEM based on the split-node approach.

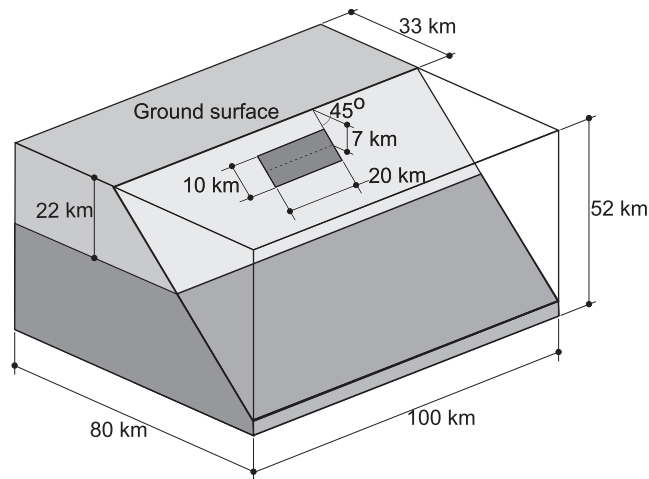


Figure 17. Model geometry for an inclined fault. The model is cut along the fault plane (dark grey) and consists of an upper elastic layer (light grey) and a lower viscous layer (dark grey).

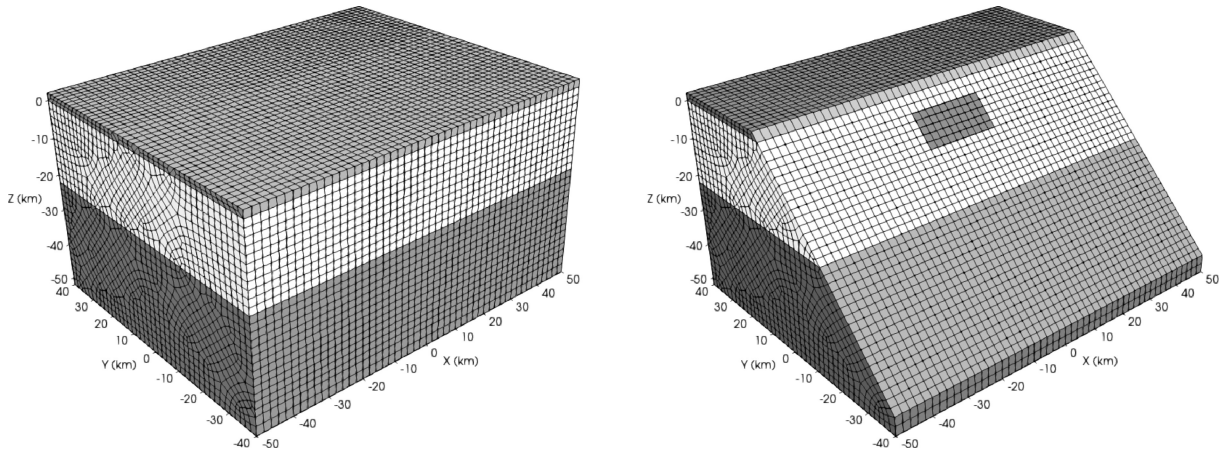


Figure 18. Left: spectral-element mesh of an inclined fault model. Right: the model is cut along the fault plane (dark grey). A transition layer is added on top of the free surface (light grey).

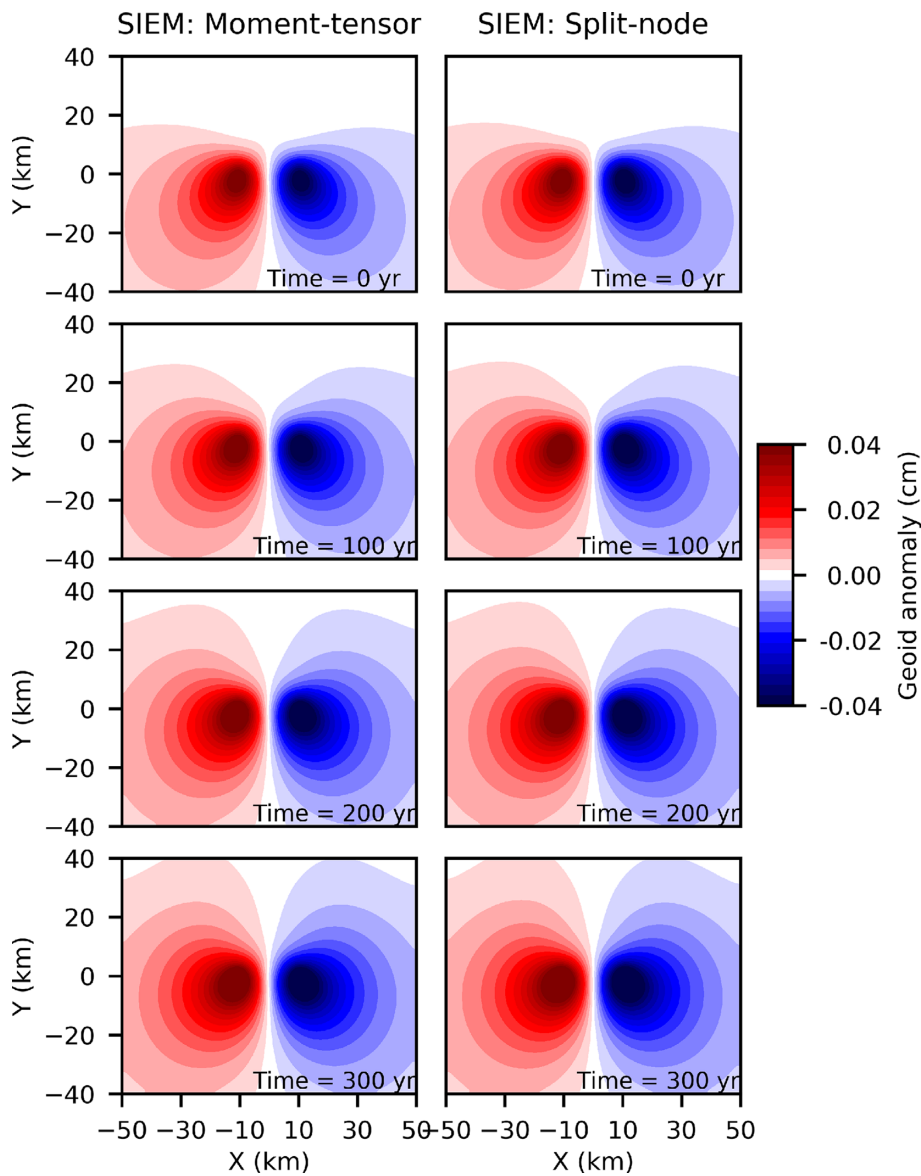


Figure 19. Geoid anomaly for an inclined strike-slip fault computed on the free surface at 0, 100, 200 and 300 yr after the earthquake (top to bottom). Left column: SIEM using the moment-density tensor approach. Right column: SIEM using the split-node approach.

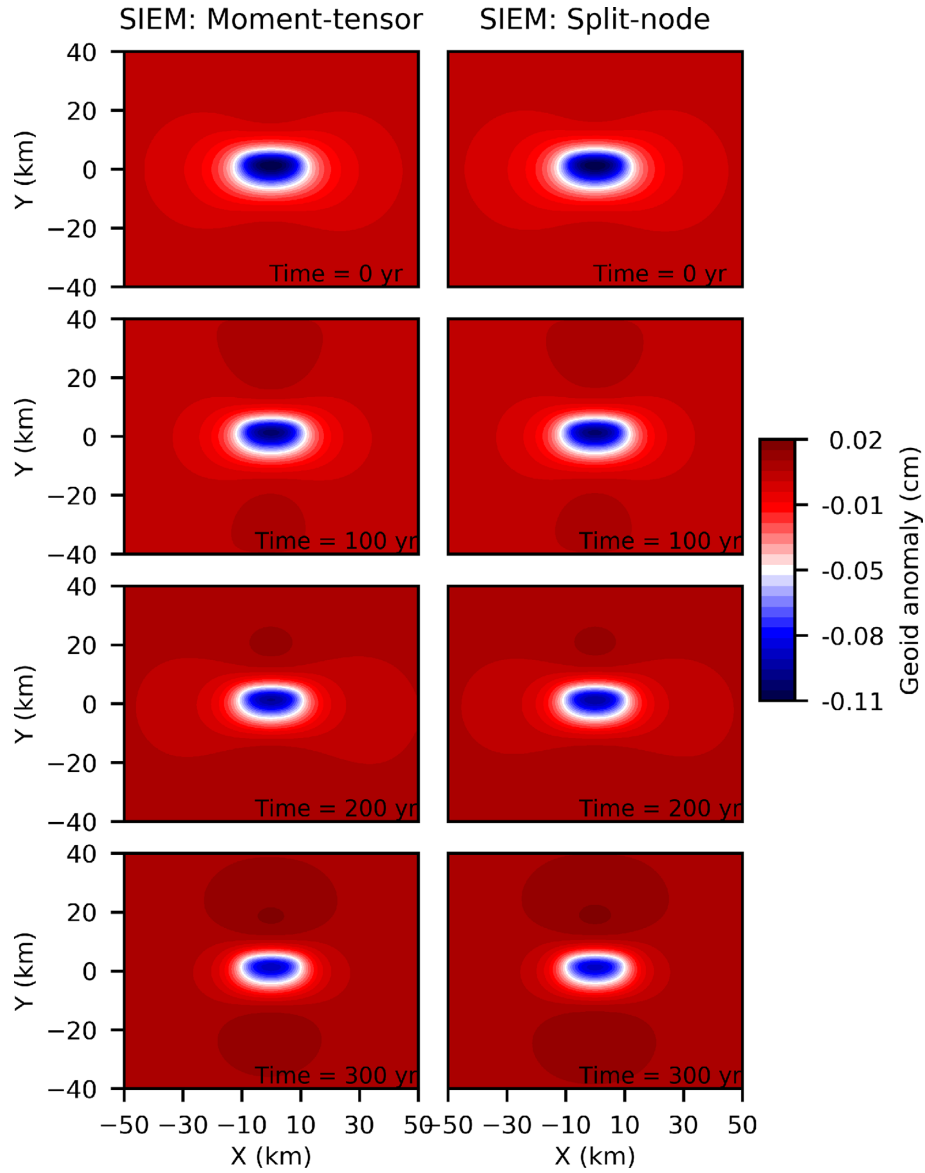


Figure 20. Geoid anomaly computed on the free surface for an inclined thrust fault at times of 0, 100, 200 and 300 yr post-earthquake (top to bottom). Left column: SIEM with moment-density tensor approach. Right column: SIEM with split-node approach.

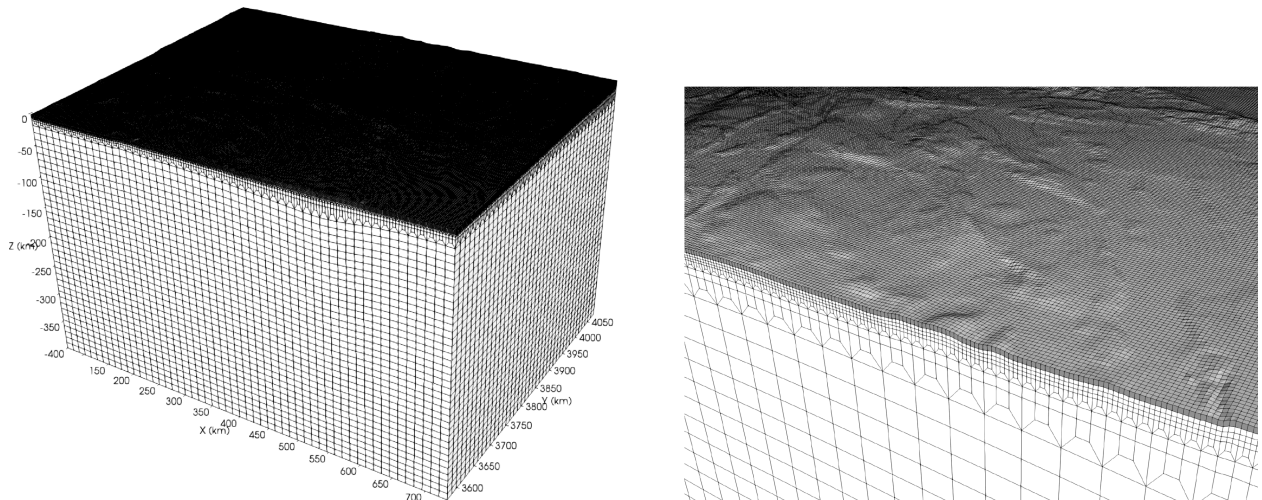


Figure 21. Left: spectral-element mesh of the 3-D Southern California model. Right: zoomed in view of the mesh. To accommodate topography with the infinite elements, a transition layer is added on top of the free surface (grey).

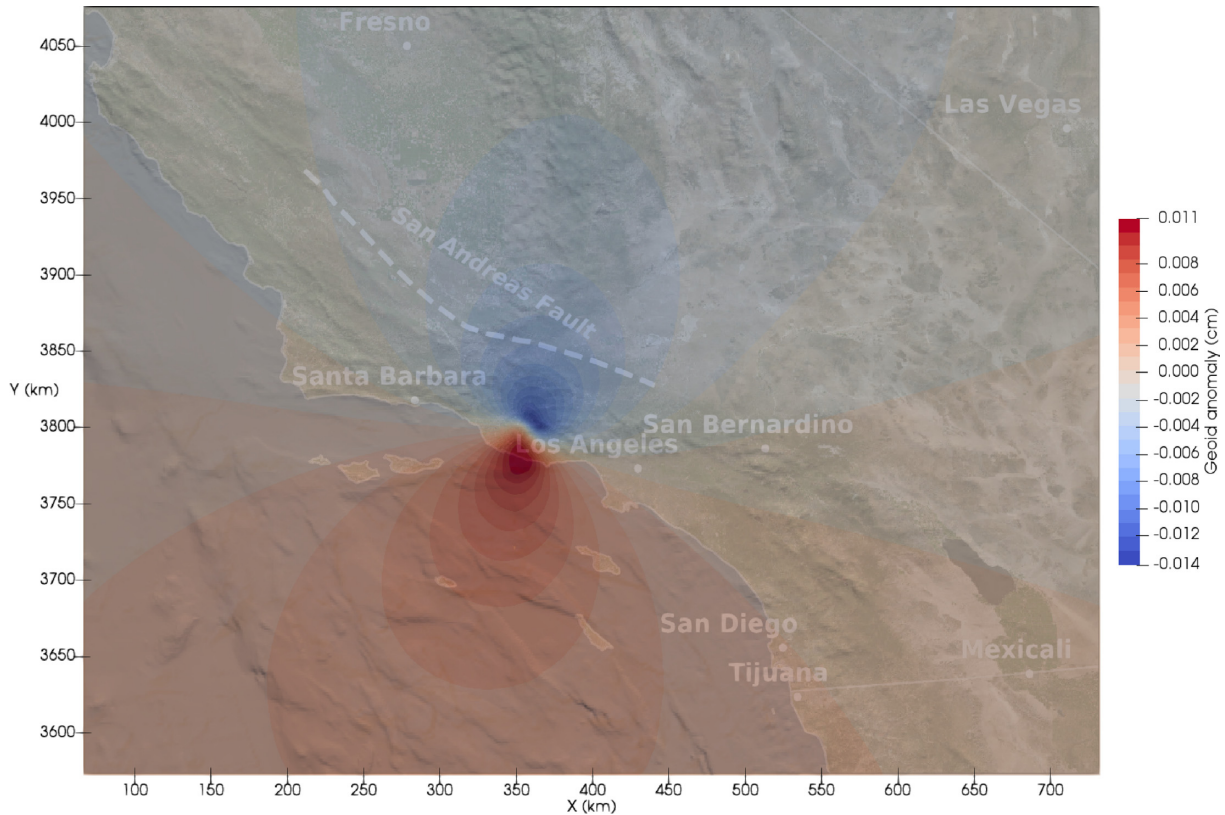


Figure 22. Geoid anomaly on the free surface for the 1994 Northridge earthquake in the 3-D Southern California model.

(right). The outer surface has 194 228 infinite elements, which comprise about 15 per cent of all elements. We use three GLL points in each direction, resulting in a total of 10 566 031 nodes and 32 832 519 degrees of freedom. It takes about 12 min on 200 processors to compute the gravity perturbations.

Fig. 22 shows a map of the geoid anomaly computed on the free surface. We observe a maximum anomaly of ≈ 0.11 mm and a minimum anomaly of ≈ -0.14 mm near the source. Although the two major lobes of the geoid anomaly are similar in appearance, the pattern near the source is complicated and asymmetric due to the complex topography and the finite rupture.

4 DISCUSSION

We successfully implemented an SIEM to simulate earthquake-induced gravity perturbations, using moment-density tensor and split-node approaches for the source implementation. Implementation of both the moment-density tensor and split-node approaches allows us to simulate complex faults in various settings. We used infinite elements to solve the unbounded Poisson/Laplace equation and to implement far-field displacement boundary conditions. The infinite-element layer requires less than 15 per cent additional memory.

We used several examples to benchmark our results against the analytical solutions for coseismic gravity perturbations. We also computed post-earthquake gravity perturbations for those examples. Benchmarks against the Okubu analytical solutions show that the method is very accurate. For viscoelastic post-earthquake simulations, the method is accurate and stable for both the moment-density tensor and the split-node methods.

Our examples show that for a given fault size and slip magnitude, the geoid anomaly and viscoelastic behaviour depend on the fault orientation and slip direction. The inclined fault dipping at 45° generates a larger geoid anomaly than the vertical fault with the same slip direction. The inclined thrust fault dipping at the same angle generates an even greater geoid anomaly. For the vertical strike-slip fault, we observe that the geoid anomaly decays with time, whereas for the 45° dipping fault the geoid anomaly increases with time. For the thrust fault with 45° dip, negative geoid anomalies decrease with time, but positive anomalies slightly increase with time.

To date, induced-gravity data have not been fully exploited to constrain earthquake source parameters, and the tools developed as part of this article may be used for such investigations. Our simulation of the 1994 Northridge earthquake demonstrates that our technique may be used for real-world applications. In this example, the calculated geoid anomaly is affected by the bathymetry and topography of the region.

For viscoelastic simulations, it is generally known that low-order isoparametric elements suffer from the so-called shear locking phenomenon, which can be alleviated by using reduced integration and/or higher order Lagrangian elements (Simo & Hughes 1998;

Zienkiewicz & Taylor 2005). It would be interesting to explore how the SIEM behaves for such phenomena in future applications. Future work will also focus on other global quasi-static and dynamic problems, such as tsunamis, glacial rebound and sea-level change.

Our package is open source and freely available via the Computational Infrastructure for Geodynamics (geodynamics.org).

ACKNOWLEDGEMENTS

We thank Stefano Zampini for his help with implementing the PETSc library, Lei Zhang and Chen Ji for providing the finite source model of the 1994 Northridge earthquake and Uno Vaaland for helping with the geodetic plot. We adapted the Okubo analytical package originally written by François Beauducel and later modified by Taco Broerse. Parallel programs were run on computers provided by the Princeton Institute for Computational Science and Engineering (PICSciE). 3-D data were visualized using the open-source parallel visualization software ParaView/VTK (www.paraview.org). 2-D snapshots were created using the open-source Python plotting library Matplotlib (www.matplotlib.org). Most of the model sketches were created using the open-source vector graphics editor Inkscape (inkscape.org). We thank David Al-Attar, an anonymous reviewer, and Editor Jean Virieux for their insightful comments, which helped to improve the manuscript.

REFERENCES

- Al-Attar, D. & Tromp, J., 2014. Sensitivity kernels for viscoelastic loading based on adjoint methods, *Geophys. J. Int.*, **196**(1), 34–77.
- Al-Attar, D. & Woodhouse, J., 2008. Calculation of seismic displacement fields in self-gravitating earth models—applications of minors vectors and symplectic structure, *Geophys. J. Int.*, **175**(3), 1176–1208.
- Angelov, T.A., 1991. Infinite elements-theory and applications, *Comput. Struct.*, **41**(5), 959–962.
- Beauducel, F., 2013. *Okubo: Gravity Change due to Shear and Tensile Faults*, MATLAB Central File Exchange.
- Beer, G. & Meek, J.L., 1981. ‘Infinite domain’ elements, *Int. J. Numer. Methods Eng.*, **17**(1), 43–52.
- Bettess, P., 1977. Infinite elements, *Int. J. Numer. Methods Eng.*, **11**(1), 53–64.
- Canuto, C., Hussaini, M.Y., Quarteroni, A. & Zang, T.A., 1988. *Spectral Methods in Fluid Dynamics*, Springer.
- Chaljub, E. & Valette, B., 2004. Spectral element modelling of three-dimensional wave propagation in a self-gravitating Earth with an arbitrarily stratified outer core, *Geophys. J. Int.*, **158**(1), 131–141.
- Chen, J.L., Wilson, C.R., Tapley, B.D. & Grand, S., 2007. GRACE detects coseismic and postseismic deformation from the Sumatra–Andaman earthquake, *Geophys. Res. Lett.*, **34**(13), L13302.
- Crawford, O., Al-Attar, D., Tromp, J. & Mitrovica, J.X., 2017. Forward and inverse modelling of post-seismic deformation, *Geophys. J. Int.*, **208**(2), 845–876.
- CUBIT, 2017. *CUBIT 15.3 User Documentation*, Sandia National Laboratories (Online; accessed 27 January 2017).
- Dahlen, F.A. & Tromp, J., 1998. *Theoretical Global Seismology*, Princeton University Press.
- Deville, M.O., Fischer, P.F. & Mund, E.H., 2002. *High-Order Methods for Incompressible Fluid Flow*, Cambridge Univ. Press.
- El-Esnawy, N.A., Akl, A.Y. & Bazaraa, A.S., 1995. A new parametric infinite domain element, *Finite Elem. Anal. Des.*, **19**(1-2), 103–114.
- Faccioli, E., Maggio, F., Paolucci, R. & Quarteroni, A., 1997. 2D and 3D elastic wave propagation by a pseudo-spectral domain decomposition method, *J. Seismol.*, **1**, 237–251.
- Gharti, H.N., & Tromp, J., 2017. A spectral-infinite-element solution of Poisson’s equation: an application to self gravity, preprint, [arXiv:1706.00855](https://arxiv.org/abs/1706.00855).
- Gharti, H.N., Komatitsch, D., Oye, V., Martin, R. & Tromp, J., 2012a. Application of an elastoplastic spectral-element method to 3D slope stability analysis, *Int. J. Numer. Methods Eng.*, **91**, 1–26.
- Gharti, H.N., Oye, V., Komatitsch, D. & Tromp, J., 2012b. Simulation of multistage excavation based on a 3D spectral-element method, *Comput. Struct.*, **100–101**, 54–69.
- Gharti, H.N., Langer, L., Roth, M., Tromp, J., Vaaland, U. & Yan, Z., 2017. MeshAssist: an open-source and cross-platform meshing assistant tool, doi:10.5281/zenodo.883448.
- Gharti, H.N., Tromp, J. & Zampini, S., 2018. Spectral-infinite-element simulations of gravity anomalies, *Geophys. J. Int.*, **215**(2), 1098–1117.
- Gharti, H.N., Langer, L. & Tromp, J., 2019. Spectral-infinite-element simulations of coseismic and post-earthquake deformation, *Geophys. J. Int.*, **216**(2), 1364–1393.
- Kumar, P., 1985. Static infinite element formulation, *J. Struct. Eng.*, **111**(11), 2355–2372.
- Latychev, K., Mitrovica, J.X., Tromp, J., Tamisiea, M.E., Komatitsch, D. & Christara, C.C., 2005. Glacial isostatic adjustment on 3-D Earth models: a finite-volume formulation, *Geophys. J. Int.*, **161**(2), 421–444.
- Matsuo, K. & Heki, K., 2011. Coseismic gravity changes of the 2011 Tohoku-Oki earthquake from satellite gravimetry, *Geophys. Res. Lett.*, **38**(7), L00G12.
- Mavriplis, C., 1989. Laguerre polynomials for infinite-domain spectral elements, *J. Comput. Phys.*, **80**(2), 480–488.
- Medina, F. & Taylor, R.L., 1983. Finite element techniques for problems of unbounded domains, *Int. J. Numer. Methods Eng.*, **19**(8), 1209–1226.
- Montagner, J.-P. *et al.*, 2016. Prompt gravity signal induced by the 2011 Tohoku-Oki earthquake, *Nat. Commun.*, **7**, 13349.
- Okubo, S., 1991. Potential and gravity changes raised by point dislocations, *Geophys. J. Int.*, **105**(3), 573–586.
- Okubo, S., 1992. Gravity and potential changes due to shear and tensile faults in a half-space, *J. geophys. Res.*, **97**(B5), 7137–7144.
- Ozawa, S., Nishimura, T., Munekane, H., Suito, H., Kobayashi, T., Tobita, M. & Imakiire, T., 2012. Preceding, coseismic, and postseismic slips of the 2011 Tohoku earthquake, Japan, *J. geophys. Res.*, **117**(B7), B07404.
- Panet, I. *et al.*, 2007. Coseismic and post-seismic signatures of the Sumatra 2004 December and 2005 March earthquakes in GRACE satellite gravity, *Geophys. J. Int.*, **171**(1), 177–190.
- Patera, A.T., 1984. A spectral element method for fluid dynamics: laminar flow in a channel expansion, *J. Comput. Phys.*, **54**, 468–488.
- Peltier, W., Farrell, W. & Clark, J., 1978. Glacial isostasy and relative sea level: a global finite element model, *Tectonophysics*, **50**(2-3), 81–110.
- Peter, D. *et al.*, 2011. Forward and adjoint simulations of seismic wave propagation on fully unstructured hexahedral meshes, *Geophys. J. Int.*, **186**(2), 721–739.
- Pollitz, F.F., 1997. Gravitational viscoelastic postseismic relaxation on a layered spherical Earth, *J. geophys. Res.*, **102**(B8), 17 921–17 941.
- Pollitz, F.F., 2014. Post-earthquake relaxation using a spectral element method: 2.5-D case, *Geophys. J. Int.*, **198**(1), 308–326.
- Rundle, J.B., 1980. Static elastic-gravitational deformation of a layered half space by point couple sources, *J. geophys. Res.*, **85**(B10), 5355–5363.
- Seriani, G. & Oliveira, S.P., 2008. Dispersion analysis of spectral-element methods for elastic wave propagation, *Wave Motion*, **45**, 729–744.
- Simo, J.C. & Hughes, T.J.R., 1998. *Computational Inelasticity*, Springer.
- Spada, G. *et al.*, 2004. Modeling earth’s post-glacial rebound, *EOS, Trans. Am. geophys. Un.*, **85**(6), 62–64.
- Sun, W. & Okubo, S., 1993. Surface potential and gravity changes due to internal dislocations in a spherical earth—I. Theory for a point dislocation, *Geophys. J. Int.*, **114**(3), 569–592.

- Sun, W. & Okubo, S., 1998. Surface potential and gravity changes due to internal dislocations in a spherical earth—II. Application to a finite fault, *Geophys. J. Int.*, **132**(1), 79–88.
- Takeuchi, H. & Saito, M., 1972. Seismic surface waves, *Seismology: Surface Waves and Earth Oscillations*, in *Methods in Computational Physics: Advances in Research and Applications*, Vol. **11**, pp. 217–295, ed. Bolt, B.A., Elsevier.
- Tape, C., Liu, Q., Maggi, A. & Tromp, J., 2009. Adjoint tomography of the southern California crust, *Science*, **325**(5943), 988–992.
- Tromp, J. & Mitrovica, J.X., 1999a. Surface loading of a viscoelastic Earth—I. General theory, *Geophys. J. Int.*, **137**(3), 847–855.
- Tromp, J. & Mitrovica, J.X., 1999b. Surface loading of a viscoelastic Earth—II. Spherical models, *Geophys. J. Int.*, **137**(3), 856–872.
- Tromp, J., Komatitsch, D. & Liu, Q., 2008. Spectral-element and adjoint methods in seismology, *Commun. Comput. Phys.*, **3**(1), 1–32.
- Tsynkov, S.V., 1998. Numerical solution of problems on unbounded domains. A review, *Appl. Numer. Math.*, **27**(4), 465–532.
- Wald, D.J., Heaton, T.H. & Hudnut, K.W., 1996. The slip history of the 1994 Northridge, California, earthquake determined from strong-motion, teleseismic, GPS, and leveling data, *Bull. seism. Soc. Am.*, **86**(1B), S49–S70.
- Wang, L., Shum, C.K., Simons, F.J., Tapley, B. & Dai, C., 2012. Coseismic and postseismic deformation of the 2011 Tohoku-Oki earthquake constrained by GRACE gravimetry, *Geophys. Res. Lett.*, **39**(7), L07301.
- Whipple, K.X., Shirzaei, M., Hodges, K.V. & Ramon Arrowsmith, J., 2016. Active shortening within the Himalayan orogenic wedge implied by the 2015 Gorkha earthquake, *Nat. Geosci.*, **9**, 711–717.
- Zhong, S., Paulson, A. & Wahr, J., 2003. Three-dimensional finite-element modelling of Earth's viscoelastic deformation: effects of lateral variations in lithospheric thickness, *Geophys. J. Int.*, **155**(2), 679–695.
- Zienkiewicz, O.C. & Taylor, R.L., 2005. *The Finite Element Method for Solid and Structural Mechanics*, Elsevier Butterworth-Heinemann.
- Zienkiewicz, O.C., Emson, C. & Bettess, P., 1983. A novel boundary infinite element, *Int. J. Numer. Methods Eng.*, **19**(3), 393–404.